Nano Research

ISSN 1998-0124 CN 11-5974/O4
https://doi.org/10.26599/NR.2026.94908745

Research Article

Vapor-phase self-assembly of orientation-controlled amino acid nanorod arrays for energy harvesting

Ying Tang[1,2,§], Pei Du[2,§], Shuaikang Zhou[2], Tong Wu[2], Weiqiang Fan[2], Haoyu Wang[2], Ehud Gazit[3], Rusen Yang[1](✉)

[1] School of Physics, Xidian University, Xi'an 710071, China

[2] School of Advanced Materials and Nanotechnology, Xidian University, Xi'an 710071, China

[3] Department of Molecular Microbiology and Biotechnology, George S. Wise Faculty of Life Sciences, Tel Aviv University, Tel Aviv 6997801, Israel

[§] Ying Tang and Pei Du contributed equally to this study.

Nano Res., **Just Accepted Manuscript** • https://doi.org/10.26599/NR.2026.94908745

https://www.sciopen.com/journal/1998-0124 on Apr. 17, 2026

Just Accepted

Vapor-phase self-assembly of orientation-controlled amino acid nanorod arrays for energy harvesting

Ying Tang, Pei Du, Shuaikang Zhou, Tong Wu, Weiqiang Fan, Haoyu Wang, Ehud Gazit, Rusen Yang*

School of Physics, Xidian University, Xi'an 710071, China
School of Advanced Materials and Nanotechnology, Xidian University, Xi'an 710071, China
Department of Molecular Microbiology and Biotechnology, George S. Wise Faculty of Life Sciences, Tel Aviv University, Tel Aviv 6997801, Israel

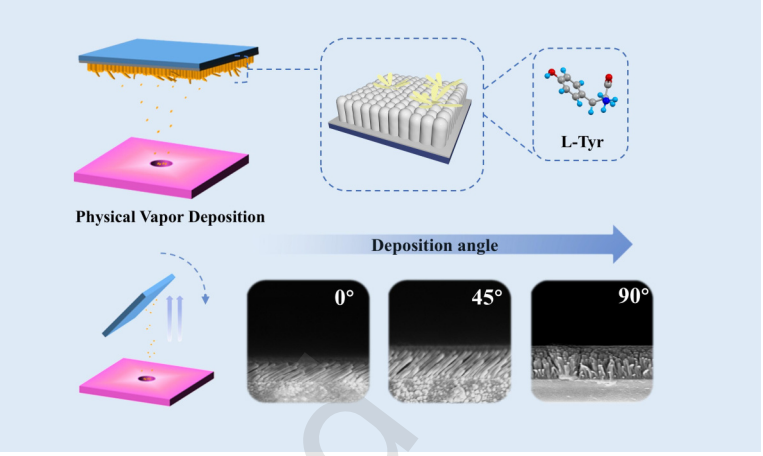

Amino acid self-assembly mechanism in vapor and the orientation control strategy for aligned nanorod arrays.

Rusen Yang, https://yang.xidian.edu.cn/

Nano Research

ISSN 1998-0124 CN 11-5974/O4
https://doi.org/10.26599/NR.2026.94908745

Research Article

Vapor-phase self-assembly of orientation-controlled amino acid nanorod arrays for energy harvesting

Ying Tang[1,2,§], Pei Du[2,§], Shuaikang Zhou[2], Tong Wu[2], Weiqiang Fan[2], Haoyu Wang[2], Ehud Gazit[3], and Rusen Yang[1] (✉)

[1] *School of Physics, Xidian University, Xi'an 710071, China*
[2] *School of Advanced Materials and Nanotechnology, Xidian University, Xi'an 710071, China*
[3] *Department of Molecular Microbiology and Biotechnology, George S. Wise Faculty of Life Sciences, Tel Aviv University, Tel Aviv 6997801, Israel*
[§] *Ying Tang and Pei Du contributed equally to this study.*

Received: 13 February 2026 / **Revised:** 13 April 2026 / **Accepted:** 17 April 2026

ABSTRACT

Biomolecules can form micro- and nanoscale structures with unique physicochemical properties. These structures tend to grow randomly in solution or on a substrate, and the lack of orientation control stems from a limited understanding of the self-assembly process, hindering their applications. Here, we achieve aligned, uniform nanorod arrays of aromatic amino acids via an electric-field-assisted physical vapor deposition process. The electric driving force and non-covalent intermolecular interactions work synergistically in biomolecular self-assembly. The vapor-deposition angle controls the stacking direction of tyrosine, phenylalanine, and levodopa, and a dynamic transition from vertical columnar crystals to horizontal needle-like epitaxial growth is observed. The good mechanical properties and piezoelectric response enable the fabrication of piezoelectric nanogenerators for environmental energy harvesting. The present work provides a new direction for the controlled growth of smart biomaterials and promotes their practical applications.

KEYWORDS

physical vapor deposition, aromatic amino acids, Stranski–Krastanov growth, ordered array, piezoelectricity, nanogenerator

1 Introduction

Supramolecular self-assembly of organic molecules has garnered significant attention in the field of smart materials, in which small molecules such as peptides or amino acids spontaneously form ordered structures via non-covalent interactions[1-15]. In recent years, amino acids have emerged as promising biological and biomimetic materials due to their low cost, ease of fabrication, and biodegradability [16-20]. Their thermal stability, mechanical rigidity, and piezoelectric properties endow them with broad application prospects[21-29]. However, fundamental questions regarding the controlled self-assembly of amino acids remain unresolved, particularly those concerning the formation of uniform, oriented nanostructures with enhanced properties.

The solution-based method is the most widely adopted strategy for supramolecular self-assembly and has yielded various nanostructures from different materials [30-35]. However, the variation in the morphology of the nanostructures in solution and the inevitable defects introduced by the low-temperature process remain a challenge [36]. Physical vapor deposition (PVD) offers a viable approach for controlled material fabrication under vacuum at elevated temperatures, enabling the production of nanomaterials with high crystallinity and few defects[37-39]. However, studies on PVD-grown amino acid crystals remain relatively scarce, and a lack of understanding of their growth mechanisms hinders the further development of amino acid-based nanomaterials.

Inspired by a modified Stranski-Krastanov (S-K) growth mechanism for biomolecule self-assemblies [40], we developed an effective growth strategy for uniform nanowire arrays. By modulating the substrate temperature, deposition angle, and in-situ electric field, we achieved controllable fabrication of large-area, highly oriented aromatic amino acid arrays with improved properties. Hirshfeld surface analysis and density functional theory (DFT) calculations revealed a synergistic effect of intermolecular interactions during assembly. We proposed a hybrid growth mechanism to elucidate the dynamic transition from vertical columnar nuclei to horizontal needle-like epitaxial structures (Fig. 1a). The amino acid arrays exhibited excellent mechanical properties and piezoelectric characteristics, and nanogenerators were thus constructed from L-Tyr arrays, demonstrating their

Address correspondence to rsyang@xidian.edu.cn

potential for device applications.

2 Experimental

Materials. L-Phenylalanine (L-Phe), L-tyrosine (L-Tyr), L-Tryptophan(L-Trp), and L-DOPA (purity: 99%) were purchased from Aladdin Reagent Co., Ltd. (Shanghai, China). Ethanol (EtOH) was obtained from Sinopharm Chemical Reagent Co., Ltd. (China). All materials were used directly without further purification. Deionized water was prepared using a water purification system (Sartorius Smart-N Ultra-Water System; Sartorius AG, Göttingen, Germany).

Fabrication of Aromatic Amino Acid Arrays. L-Phe, L-Tyr, L-Trp, and L-DOPA powders were weighed and placed in a custom-designed PVD system. Silicon wafers (1 cm × 1 cm) were used as substrates, with their height and tilting angle relative to the heating source adjustable. The sample stage was electrically insulated and negatively biased during deposition. The distance between the source furnace and the sample stage was fixed at 5 cm, establishing a directional electric field between them. The detailed experimental parameters are summarized in Table S3. When the vacuum level reached 5×10^{-5} Pa, the system was heated to a preset temperature and maintained for a specific period. The aromatic amino acids underwent sublimation and deposited onto the substrates, completing the self-assembly process. Large-area aromatic amino acid arrays were formed on the substrate.

Fabrication of Nanogenerators Based on L-Tyr Arrays. A silver film was uniformly deposited on a silicon substrate via magnetron sputtering. L-Tyr crystal arrays were directly grown on the silver electrode surface via PVD. A PDMS protective layer was spin-coated onto the array surface. Another silicon wafer coated with a silver layer was used as the top cover plate. The edges were sealed with Kapton tape, completing the fabrication of a nanogenerator.

Characterization. A field-emission SEM (SU-8600) was used to examine the morphology of the aromatic amino acid array, producing top-view and cross-sectional SEM images. The crystal structure of the aromatic amino acid array was studied by XRD (D8 DISCOVER) using Cu target radiation. The molecular structures of the samples were investigated using a Fourier-transform infrared (FT-IR) spectrometer (Thermo Fisher Scientific, Nicolet iS50). The thermal degradation behavior of the aromatic amino acid was evaluated by thermogravimetric analysis (Netzsch STA449F5) under an air atmosphere at a heating rate of $10°C \cdot min^{-1}$. The elastic modulus of tyrosine crystals was measured using nanoindentation with an atomic force microscope (Cypher ES), and the piezoelectric effect was measured using piezoresponse force microscopy (PFM). Scanning Kelvin Probe Microscopy (SKPM) was used to eliminate the influence of substrate, background, and tip static charges on the intrinsic piezoelectricity. The nanogenerator's performance was measured using an electrometer (Keithley 6517b). To reduce possible triboelectric interference during nanogenerator testing, a thin aluminum layer was introduced into the device structure as a shielding layer to effectively dissipate friction-induced charges generated during the measurement process.

3 Results and discussion

Under vacuum conditions, aromatic amino acids were sublimated and deposited onto Ag-coated silicon substrates (Fig. 1a). The amino acids selected in this study, L-Phe, L-Tyr, and L-DOPA, share similar chemical structures (Fig. 1b), and their different number of hydroxyl groups on the aromatic ring enable the investigation of the influence of the molecular structure and non-covalent bonding on the self-assembly process. SEM images show distinct morphologies of the film from a prolonged PVD process of three amino acids (Fig. S1). Although the number of functional groups and the relative contributions of noncovalent interactions play important roles in array growth, a deeper understanding of the structure–morphology relationship still requires further theoretical calculations and analysis, because this process is closely related to molecular orientation, packing, hydrogen-bonding interactions, and the cooperative or competitive effects of multiple weak interactions in three-dimensional space[41]. However, all three aromatic amino acids formed similar columnar structures during the early stages of self-assembly (Fig. 1c–e). Top-view SEM images showed fine, uniformly distributed nanowires arranged in a dense, ordered manner, indicating strong intermolecular interactions during deposition. Cross-sectional SEM images further confirmed the vertically aligned, uniform columnar architecture of the amino acid self-assemblies, indicating a pronounced directional growth during deposition.

As shown in Fig. 2a–c, the XRD patterns agree with the crystal structures of L-Phe, L-Tyr, and L-DOPA. To further investigate the molecular structural features, the bonding states of the three amino acids were analyzed using FT-IR spectroscopy. The characteristic peaks at 1455 cm^{-1} and 1603 cm^{-1} are attributed to aromatic skeletal vibrations (Fig. 2d–f). The absorption peak at 530 cm^{-1} indicates the presence of carboxyl groups (–COOH), while the broad absorption band around 3250 cm^{-1} confirms the existence of amino groups ($–NH_2$) and the formation of intermolecular hydrogen bonds. Hydrogen bonding plays a critical role in the self-assembly of molecules, stabilizing the molecule stacking and facilitating the formation of ordered structures. It is noteworthy that the PVD process temperature is precisely

controlled to prevent

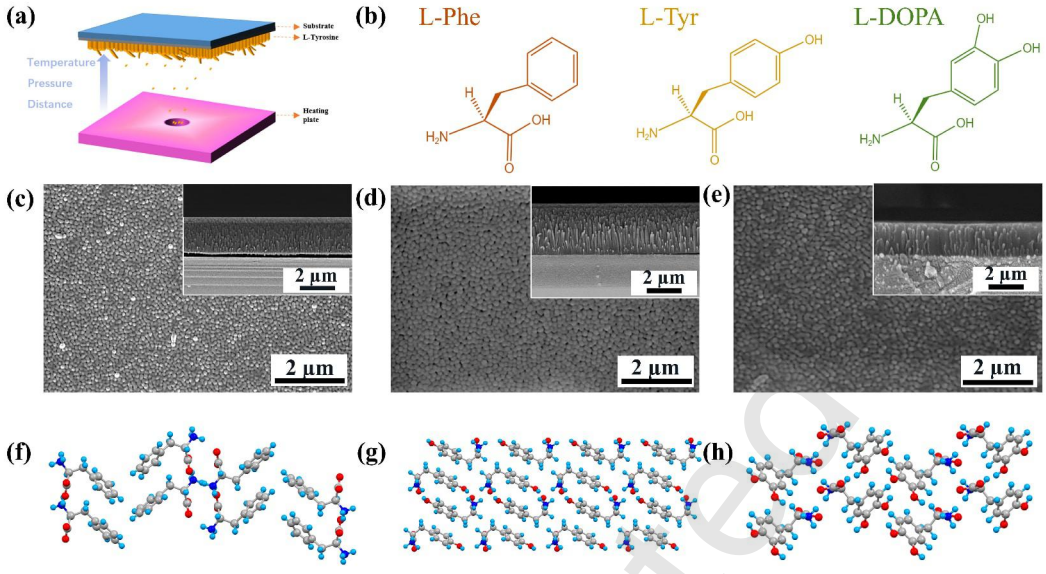

Figure 1. Growth processes, morphologies, and crystal structures of self-assemblies of aromatic amino acids and their derivatives. (a) Schematic illustration of the growth of aromatic amino acid arrays via PVD. (b) Chemical structures of L-Phe, L-Tyr, and L-DOPA. (c–e) SEM images of assembled structures of (c) L-Phe, (d) L-Tyr, and (e) L-DOPA. (f–h) Crystal structures of (f) L-Phe, (g) L-Tyr, and (h) L-DOPA. Color code: gray, C; dark blue, N; red, O.

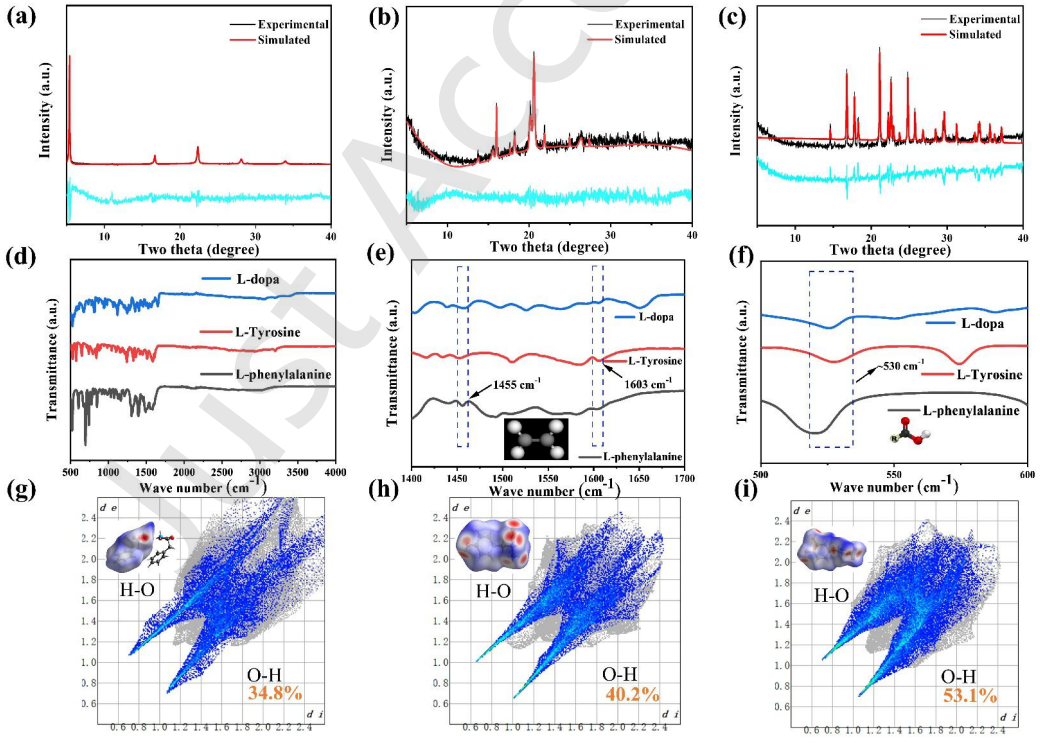

Figure 2. Structure characterization of self-assemblies of aromatic amino acids and their derivatives via PVD. (a–c) XRD patterns of nanowire arrays of (a) L-Phe, (b) L-Tyr, and (c) L-DOPA. (d–f) FT-IR spectra of nanowire arrays of (d) L-Phe, (e) L-Tyr, and (f) L-DOPA. (e, f) Magnified views of the FT-IR spectra of nanowire arrays. (g–i) 2D fingerprint plots of nanowire arrays of (g) L-Phe, (h) L-Tyr, and (i) L-DOPA. The percentage of the O-H interaction is also provided.

thermal decomposition of amino acids and to preserve their chemical stability.

We performed Hirshfeld surface analysis using DFT to investigate the critical role of non-covalent interactions, such as hydrogen bonding, van der Waals forces, and π–π stacking, in the self-assembly process. The two-dimensional fingerprint plots with the normalized contact distance (d $_{or}$) visualize the distribution and strength of various intermolecular interactions, as shown in

Fig.2g-i. L-Phe, which lacks hydroxyl groups on the benzene ring, exhibits fewer O–H interactions (34.8% of the total interaction) than L-Tyr (40.2%). In contrast, L-DOPA molecules have even more hydroxyl groups and exhibit stronger O–H interactions (53.1%), indicating that hydrogen bonding serves as the dominant driving force in its self-assembly. The proportions of C–H interactions for L-Phe, L-Tyr, and L-DOPA are 19.0%, 17.7%, and 18.2%, respectively.These interactions involve C–H···π bonding and also play an essential role in molecular self-assembly (Fig. S2–S4). The π–π stacking mediated by the conjugated π systems of the benzene rings synergizes with hydrogen bonding to promote ordered molecular alignment and facilitate the formation of stable self-assembled structures.

The PVD temperature and deposition angle play crucial roles in crystal nucleation and growth, and L-Tyr arrays self-assembled at different substrate temperatures and tilting angles were investigated. The substrate was first mounted with its surface facing the heating crucible, and we refer to this as a 90° deposition angle. As shown in Fig. 3a, dense columnar structures are formed at a temperature as low as 40 °C. As the substrate temperature increases, needle-like structures start to form in the horizontal direction (Fig. 3b). When the temperature is raised to 80 °C, a large number of needle-shaped structures are found (Fig. 3c). The transition from vertical growth of nanowires to lateral growth of much larger needle-like structures is likely due to the temperature-dependent surface mobility of L-Tyr molecules. At lower temperatures, the strong intermolecular interactions (e.g., hydrogen bonding and π–π interactions) and low molecular mobility favor the local self-assembly of nanowires. In comparison, molecules can migrate long distances at high temperatures, and the formation of large, laterally oriented need-like structures becomes possible.

The deposition angle was found to influence the self-assembly behavior. As shown in Fig. 3d, at a deposition angle of 90°, L-Tyr forms a dense, uniform, and aligned nanowire film on the substrate. When the deposition angle was reduced to 45° (Fig. 3e), the columnar structures became shorter and tilted, losing their vertical alignment. Top-view observations revealed an increased spacing between nanowires compared to the film deposited at 90°, which may be attributed to the expanded diffusion range of molecules under oblique deposition, thereby reducing local aggregation. When the deposition angle was 0° (Fig. 3f), the film became flatter, with nanowires oriented primarily parallel to the substrate surface, yielding more homogeneous, smoother thin films. The influence of deposition angle on the morphology of aromatic amino acid self-assembly can be explained by the "shadow effect". During non-vertical deposition, certain regions are shadowed and cannot receive incoming molecules, leading to significant changes in the final deposited morphology.

Electric fields were applied during the PVD process, and their effects on amino acid self-assembly were examined. As a zwitterionic molecule, L-Tyr possesses a positively charged amino group and negatively charged carboxyl and hydroxyl groups. Consequently, L-Tyr molecules respond to the external electric field during self-assembly. Under a positive electric field perpendicular to the substrate surface, the positively charged amino groups tend to be exposed on the top surface. In the absence of an electric field, L-Tyr molecules can form a relatively uniform and dense nanostructure with random orientation. However, when a DC bias of 1 kV is applied under the same PVD conditions, partial snowflake-like structures begin to appear, indicating that the external electric field already induces directional modulation of the

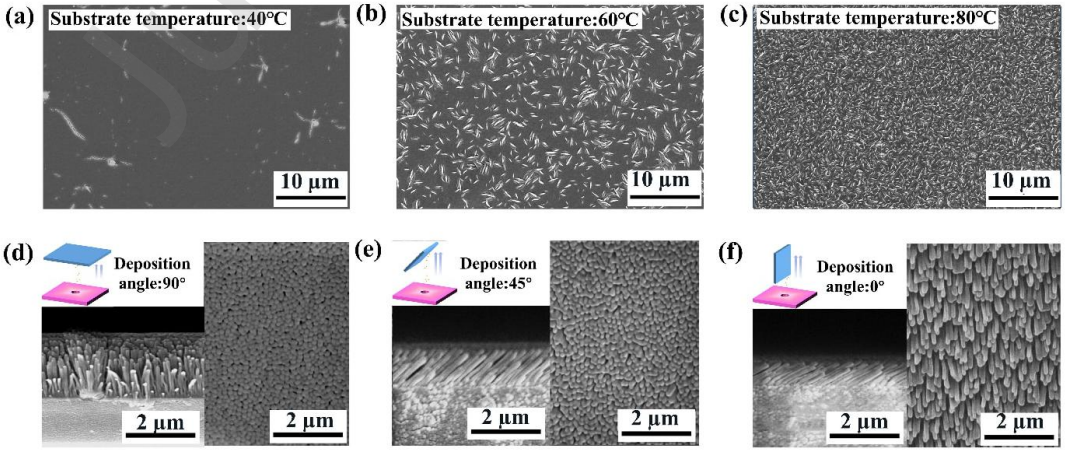

Figure 3. Effects of the substrate temperature and deposition angle on the self-assembly of L-Tyr. Top-view SEM images of L-Tyr deposited on substates at (a) 40 °C, (b) 60 °C, and (c) 80 °C; Cross-sectional view (Left) and Top view (Right) SEM images of L-Tyr deposited at different angles of (d) 90°, (e) 45°, and (f) 0°.

Nano Research
ISSN 1998-0124 CN 11-5974/O4
https://doi.org/10.26599/NR.2026.94908745

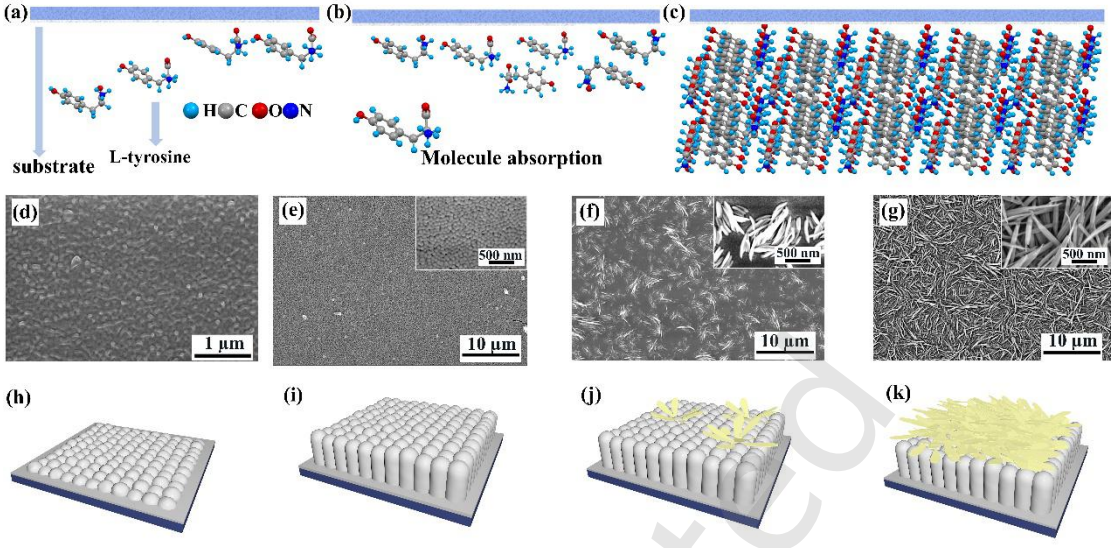

Figure 4. Self-assembly mechanism of L-Tyr via physical vapor deposition. (a–c) Molecular packing process of L-Tyr. (d–g) Top-view SEM images of L-Tyr self-assemblies at different growth stages. (h–k) Schematic diagram showing the simulated growth of L-Tyr corresponding to images in (d-g).

self-assembly process. As the applied bias is further increased to 2 kV, the morphology of L-Tyr undergoes a much more pronounced transformation, and a large number of radially symmetric structures with distinct directional features emerge, resembling snowflake- or stellate-like patterns (Fig. S5). The polar molecules tend to align with the electric field, and the driving force is strong enough to overcome thermal fluctuations and facilitate directional growth. The combined effect of intermolecular interactions governs self-assembly behavior, and how exactly the electric force affects the nucleation and crystal growth processes is worth further investigation.

We carefully investigated the different PVD stages of L-Tyr and the effects of growth parameters on self-assembled nanowires. We proposed a hybrid mechanism combining Stranski-Krastanov (SK) and Vollmer-Weber (VW) growth, which was also confirmed in the growth of other amino acids, such as L-Phe and L-DOPA (Figure 4). As shown in Fig. 4a–c, during the PVD process, L-Tyr molecules are vaporized and transported to the substrate. They then adsorb onto the substrate surface through intermolecular interactions such as hydrogen bonding and π–π stacking, gradually accumulating to form an initial molecular layer. The molecules stack in an orderly manner to match the substrate at the expense of elastic deformation energy. When the elastic strain exceeds the adhesion forces within the stacked-molecule layer, islands form, following the S-K growth model (Fig. 4d, 4h).

The incoming molecule adsorbs onto these islands, initiating homoepitaxial growth (Fig. 4e, 4i). As deposition proceeds, molecules aggregate directionally via hydrogen bonding and π–π interactions, gradually forming vertically aligned columnar structures that correspond to the Wulff construction. This growth direction is determined by the direction of incoming molecules, as confirmed in Fig. 3. In the later self-assembly stage, the substrate effect is negligible. Vertical growth slows, while a new nucleus forms on the top surface and begins to grow laterally in random directions (Fig. 4f, 4j). Owing to surface energy anisotropy, the orientation of aromatic rings favors specific crystal facets with lower energy and higher stability, promoting preferential extension of the needle-like tips along high surface energy directions (Fig. 4g, 4k), closely following a V-W growth mechanism.

Atomic force microscopy (AFM) nanoindentation was employed to investigate the influence of molecular packing on the mechanical properties of amino acid crystals. The microcantilever probe was positioned on the crystal surface and brought into contact with the sample, with an indentation depth of less than 15 nm, then immediately retracted. At the same time, force-displacement data were recorded synchronously during loading and unloading. The unloading curve was fitted using the Hertz contact model, yielding a Young's modulus of 16.96 ± 0.05 GPa in the thickness direction for L-Tyr (Fig. 5a), indicating excellent mechanical properties. This result shows strong agreement with DFT calculations (Table S1), demonstrating that the assembly formed through π–π stacking and hydrogen bonding in L-Tyr molecules effectively resists external deformation. Furthermore, thermogravimetric analysis (TGA) revealed that L-Tyr maintains thermal stability up to approximately 300 °C (Fig. 5b), supporting its capability for engineering applications.

Nano Research

ISSN 1998-0124 CN 11-5974/O4
https://doi.org/10.26599/NR.2026.94908745

Research Article

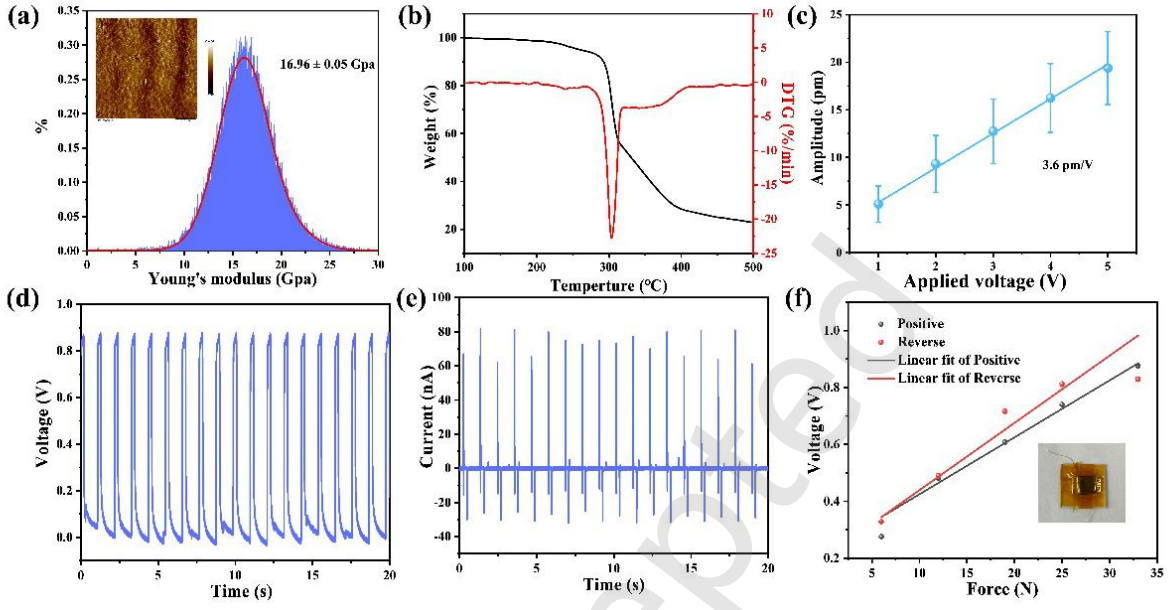

Figure 5. Characterization of PVD-based L-Tyr self-assemblies. (a) Young's modulus, (b) thermal stability, and (c) piezoelectric constant of L-Tyr self-assemblies, (d) open-circuit voltage under 33 N mechanical force, (e) short-circuit current under 33 N mechanical force, and (f) linear fitting of open-circuit voltage versus applied force of an L-Tyr-based nanogenerator. Inset in (f) is an optical image of the device.

To characterize the influence of hydrogen bonding on the surface potential of these crystals, the electrostatic potential on the Hirshfeld surface was calculated. The Tonto program and the HF method were employed in the computation, generating corresponding electrostatic potential maps based on the crystal packing structures (Fig. S6). The results indicate that all crystals exhibit negative electrostatic potential near carboxyl and hydroxyl groups (red regions), and positive electrostatic potential near amino groups (blue regions). The electrostatic potential electron density of L-Phe ranges from -0.2123 to 0.2747 $e \cdot au^{-3}$, with an average of -0.0001 $e \cdot au^{-3}$. The average electrostatic potential of L-Tyr and L-DOPA is 0.0023 $e \cdot au^{-3}$ and 0.0088 $e \cdot au^{-3}$, respectively. Tyrosine and DOPA exhibit weak positive polarity, whereas phenylalanine shows weak negative polarity. This difference originates from charge compensation among amino, hydroxyl, indole, carboxyl, and benzene ring C–H groups in the crystals. Due to stronger H–O contacts and relatively weaker C–H interactions, DOPA demonstrates higher positive polarity, further validating differences in hydrogen bonding and π-bond interactions among the various amino acids.

The piezoelectric property of the L-Tyr self-assembly arises from its non-centrosymmetric crystal structure. The elastic stiffness tensor **C**, piezoelectric stress coefficient tensor **e**, and piezoelectric charge coefficient tensor **d** were calculated using DFT (Table S2). The results show that the piezoelectric strain constants of L-Tyr crystals range from 4.21 to 19.6 pm/V. The piezoelectric coefficient was further characterized using PFM, with surface charge interferences excluded with the help of Kelvin Probe Force Microscopy (KPFM). By applying voltages ranging from 1–5 V and analyzing the relationship between the applied voltage and deformation, a maximum effective piezoelectric coefficient of 3.6 $pm \cdot V^{-1}$ was measured, consistent with the DFT computation (Fig. 5c).

A nanogenerator was constructed from an ordered L-Tyr array with a silver layer serving as the electrode and a PDMS layer as the protective layer. The entire device was dried at 80 °C, and copper wires were used to connect the top and bottom electrodes to an electrometer for performance measurements (Fig. 5d-f). When the device is pressed and released, the L-Tyr crystal film becomes polarized and depolarized due to the piezoelectric effect, driving current back and forth between the two electrodes (Fig. S7). Under a pressure of 33 N, the device exhibited an open-circuit voltage of 0.8 V and a short-circuit current of 110 nA (Fig. 5d, e). The load-dependent electrical output was further investigated, and a maximum output power of 95.2 nW was achieved at 2.4 MΩ; the corresponding power density is shown in Fig. S12(a). To further

evaluate the energy-storage capability of the device, capacitors with different capacitances (0.1, 0.22, 0.47, and 1 μF) were charged by the nanogenerator. The device was able to charge a 0.1 μF capacitor to 0.147 V within 5 min, demonstrating its potential for practical energy-storage applications(Fig. S12b). The cycling stability of the nanogenerator was further evaluated. The results show that the device maintains a stable output voltage of ~0.8 V over a testing period of 2000 s, demonstrating its good operational stability and reliability(Fig. S12c). The reversion connection test was conducted, and the results confirmed that the measured signals were truly from piezoelectric L-Tyr nanowires, eliminating the contribution from the contact resistance or parasitic capacitance (Fig.S8-S11)[42].Compared with previously reported amino-acid-based piezoelectric materials and nanogenerators, the PVD approach used in this work not only enables the controllable growth and orientation tuning of ordered L-tyrosine arrays, but also delivers good piezoelectric response and device output performance.(Table S4)[24, 40, 43, 44] Although the present study is mainly carried out on small-area substrates (1 cm × 1 cm), the PVD-based growth strategy is, in principle, scalable to larger areas, while its scalability and related influencing factors still require further systematic investigation.

4 Conclusions

Self-assemblies of aromatic amino acid arrays via physical vapor deposition were systematically investigated for the first time, and a hybrid growth mechanism was proposed. The substrate temperature, deposition angle, and applied electric field significantly influence the molecular stacking order, and control over the morphology and orientation of amino acid nanowires produces aligned array structures with enhanced physical properties. L-Tyr initially forms uniform, dense columnar structures on the substrate, followed by lateral epitaxial growth of needle-like structures via secondary nucleation and growth. Thanks to its ordered nanostructure with high crystallinity, the L-Tyr array exhibits excellent thermal stability and mechanical properties. A sandwich-structured piezoelectric nanogenerator was fabricated, producing an open-circuit voltage of 0.8 V and a short-circuit current of 110 nA. This study provides new insights into the structural design and performance optimization of ordered aromatic amino acid arrays, highlighting their potential for applications in energy harvesting, wearable electronics, and implantable electronic devices.

Acknowledgements

This work was supported by the National Natural Science Foundation of China (Grant No. 52361145848, No. 52192613, No. 51973170), ISF-Israel Science Foundation (Grant No. 3246/23), and the Natural Science Foundation of Shaanxi Province (Grant No. 2019JCW-17 and 2020JCW-15).

Electronic Supplementary Material: Supplementary material (SEM measurements, Hirshfeld surfaces analysis, DFT computation, and Nanogenerator measurements) is available in the online version of this article at https://doi.org/10.26599/NR.2026.94908745

References

[1] Zhang, S. Building from the bottom up. *Materials Today* **2003**, *6*, 20-27.

[2] Yan, X.;Zhu, P.; Li, J. Self-assembly and application of diphenylalanine-based nanostructures. *Chemical Society Reviews* **2010**, *39*.

[3] Tao, K.;Makam, P.;Aizen, R.; Gazit, E. Self-assembling peptide semiconductors. *Science* **2017**, *358*.

[4] Jeffrey D. Hartgerink, E. B., Samuel I. Stupp* Self-Assembly and Mineralization of Peptide. *SCIENCE* **2001**, *294*, 1684-1688.

[5] Grzybowski, G. M. W. a. B. Self-Assembly at All Scales. *SCIENCE* **2002**, *295*, 2418-2421.

[6] Gazit*, M. R. a. E. Casting Metal Nanowires within Discrete. *SCIENCE* **2003**, *300*, 625-627.

[7] T. Aida, 2 E. W. Meijer,3 S. I. Stupp4,5,6,7* Functional Supramolecular Polymers. *SCIENCE* **2012**, *Vol 335*, 813-817.

[8] Webber, M. J.;Appel, E. A.;Meijer, E. W.; Langer, R. Supramolecular biomaterials. *Nature Materials* **2015**, *15*, 13-26.

[9] Lampel, A.;Ulijn, R. V.; Tuttle, T. Guiding principles for peptide nanotechnology through directed discovery. *Chemical Society Reviews* **2018**, *47*, 3737-3758.

[10] Hendricks, M. P.;Sato, K.;Palmer, L. C.; Stupp, S. I. Supramolecular Assembly of Peptide Amphiphiles. *Accounts of Chemical Research* **2017**, *50*, 2440-2448.

[11] Reches, M.; Gazit, E. Controlled patterning of aligned self-assembled peptide nanotubes. *Nature Nanotechnology* **2006**, *1*, 195-200.

[12] Abbas, M.;Zou, Q.;Li, S.; Yan, X. Self‐Assembled Peptide‐ and Protein‐Based Nanomaterials for Antitumor Photodynamic and Photothermal Therapy. *Advanced Materials* **2017**, *29*.

[13] Wang, J.;Liu, K.;Xing, R.; Yan, X. Peptide self-assembly: thermodynamics and kinetics. *Chemical Society Reviews* **2016**, *45*, 5589-5604.

[14] Mu, R.;Zhu, D.;Abdulmalik, S.;Wijekoon, S.;Wei, G.; Kumbar, S. G. Stimuli-responsive peptide assemblies:

Design, self-assembly, modulation, and biomedical applications. *Bioactive Materials* **2024**, *35*, 181-207.

[15] Sinha, N. J.;Langenstein, M. G.;Pochan, D. J.;Kloxin, C. J.; Saven, J. G. Peptide Design and Self-assembly into Targeted Nanostructure and Functional Materials. *Chemical Reviews* **2021**, *121*, 13915-13935.

[16] Wang, H.;Feng, Z.; Xu, B. Bioinspired assembly of small molecules in cell milieu. *Chemical Society Reviews* **2017**, *46*, 2421-2436.

[17] Dou, X. Q.; Feng, C. L. Amino Acids and Peptide‐Based Supramolecular Hydrogels for Three‐Dimensional Cell Culture. *Advanced Materials* **2017**, *29*.

[18] Kim, D.;Han, S. A.;Kim, J. H.;Lee, J. H.;Kim, S. W.; Lee, S. W. Biomolecular Piezoelectric Materials: From Amino Acids to Living Tissues. *Advanced Materials* **2020**, *32*.

[19] Li, J.;Carlos, C.;Zhou, H.;Sui, J.;Wang, Y.;Silva-Pedraza, Z.;Yang, F.;Dong, Y.;Zhang, Z.;Hacker, T. A.;Liu, B.;Mao, Y.; Wang, X. Stretchable piezoelectric biocrystal thin films. *Nature Communications* **2023**, *14*.

[20] Cheng, Y.;Xu, J.;Li, L.;Cai, P.;Li, Y.;Jiang, Q.;Wang, W.;Cao, Y.; Xue, B. Boosting the Piezoelectric Sensitivity of Amino Acid Crystals by Mechanical Annealing for the Engineering of Fully Degradable Force Sensors. *Advanced Science* **2023**, *10*.

[21] Fan Yang1, 3†, Jun Li1†, Yin Long1, Ziyi Zhang1, Linfeng Wang1, Jiajie Sui1, Yutao Dong1, Yizhan Wang1, Rachel Taylor4, Dalong Ni5, Weibo Cai5, Ping Wang2,3, Timothy Hacker4, Xudong Wang1* Wafer-scale heterostructured piezoelectric bio-organic thin films. *Science* **2021**, *373*, 337–342 (2021).

[22] Zhang, Y.;Li, Q.;Wu, H.;Wang, Y.;Wang, Y.;Rencus-Lazar, S.;Zhao, Y.;Wang, J.;Mei, D.;Xu, H.;Gazit, E.; Tao, K. Racemic Amino Acid Assembly Enables Supramolecular β-Sheet Transition with Property Modulations. *ACS Nano* **2023**, *17*, 2737-2744.

[23] Ji, W.;Xue, B.;Arnon, Z. A.;Yuan, H.;Bera, S.;Li, Q.;Zaguri, D.;Reynolds, N. P.;Li, H.;Chen, Y.;Gilead, S.;Rencus-Lazar, S.;Li, J.;Yang, R.;Cao, Y.; Gazit, E. Rigid Tightly Packed Amino Acid Crystals as Functional Supramolecular Materials. *ACS Nano* **2019**, *13*, 14477-14485.

[24] Hu, T.;Lee, J. P.;Huang, P.;Ong, A. J.;Yu, J.;Zhu, S.;Jiang, Y.;Zhang, Z.;Reches, M.; Lee, P. S. Promoting Piezoelectricity in Amino Acids by Fluorination. *Advanced Materials* **2024**, *37*.

[25] Azuri, I.;Meirzadeh, E.;Ehre, D.;Cohen, S. R.;Rappe, A. M.;Lahav, M.;Lubomirsky, I.; Kronik, L. Unusually Large Young's Moduli of Amino Acid Molecular Crystals. *Angewandte Chemie International Edition* **2015**, *54*, 13566-13570.

[26] Guerin, S.;Stapleton, A.;Chovan, D.;Mouras, R.;Gleeson, M.;McKeown, C.;Noor, M. R.;Silien, C.;Rhen, F. M. F.;Kholkin, Andrei L.;Liu, N.;Soulimane, T.;Tofail, S. A. M.; Thompson, D. Control of piezoelectricity in amino acids by supramolecular packing. *Nature Materials* **2017**, *17*, 180-186.

[27] Yuan, H.;Zhang, J.;Rencus-Lazar, S.;Ren, Z.;Lin, R.;Gazit, E.; Yang, R. The engineering of molecular packing in amino acid crystals for the enhanced triboelectric effect. *Nano Energy* **2023**, *110*.

[28] Liu, S.;Yang, B.;Huo, Y.;Zhao, J.;Hu, J.;Chen, L.;Li, L.;Tan, M.-L.;Liu, P.;Cai, K.; Ji, W. Coordination-Driven Assembly Modulates the Piezoelectric Response of Bio-Inspired Amino Acid-Based Supramolecular Materials. *Journal of the American Chemical Society* **2025**, *147*, 34972-34988.

[29] Wang, Y.;Liu, S.;Li, L.;Li, H.;Yin, Y.;Rencus-Lazar, S.;Guerin, S.;Ouyang, W.;Thompson, D.;Yang, R.;Cai, K.;Gazit, E.; Ji, W. Manipulating the Piezoelectric Response of Amino Acid-Based Assemblies by Supramolecular Engineering. *Journal of the American Chemical Society* **2023**, *145*, 15331-15342.

[30] Cheng, Y.;Wang, T.;Zhu, H.;Hu, X.;Mi, J.;Li, L.;Zhang, Y.;Yang, J.;Dong, L.;Li, Y.;Sun, W.;Lu, X.;Wang, W.;Cao, Y.; Xue, B. Molecular Engineering of Amino Acid Crystals with Enhanced Piezoelectric Performance for Biodegradable Sensors. *Angewandte Chemie International Edition* **2025**, *64*.

[31] Bera, S.;Xue, B.;Rehak, P.;Jacoby, G.;Ji, W.;Shimon, L. J. W.;Beck, R.;Král, P.;Cao, Y.; Gazit, E. Self-Assembly of Aromatic Amino Acid Enantiomers into Supramolecular Materials of High Rigidity. *ACS Nano* **2020**, *14*, 1694-1706.

[32] Wang, T.;Ménard-Moyon, C.; Bianco, A. Self-assembly of amphiphilic amino acid derivatives for biomedical applications. *Chemical Society Reviews* **2022**, *51*, 3535-3560.

[33] Zhang, J.;Wang, Y.;Rodriguez, B. J.;Yang, R.;Yu, B.;Mei, D.;Li, J.;Tao, K.; Gazit, E. Microfabrication of peptide self-assemblies: inspired by nature towards applications. *Chemical Society Reviews* **2022**, *51*, 6936-6947.

[34] Yuan, C.;Li, Q.;Xing, R.;Li, J.; Yan, X. Peptide self-assembly through liquid-liquid phase separation. *Chem* **2023**, *9*, 2425-2445.

[35] Chang, R.;Yuan, C.;Zhou, P.;Xing, R.; Yan, X. Peptide Self-assembly: From Ordered to Disordered. *Accounts of Chemical Research* **2024**, *57*, 289-301.

[36] Yin, H.;Liao, M.;Shi, Y.;Liu, Z.;Li, H.;He, S.;Zheng, Z.;Xu, L.;Tang, J.; Niu, G. Close‐to‐Equilibrium Crystallization for Large‐Scale and High‐Quality Perovskite Single Crystals. *Advanced Materials* **2025**, *37*.

[37] Lingyu Li, Y. Y., ‡ Guoliang Yang,‡ Xuming Chen,§ Benjamin S. Hsiao,§ Benjamin Chu,§ Jonathan E. Spanier,† and Christopher Y. Li*,† patterning-polyethylene-oligomers-on-carbon-nanotubes-using-physical-vapor-deposition. *Nano Letters* **2006**, *6*, 1007–1012.

[38] Gunther Richter, K. H., Daniel S. Gianola, Reiner Monig, Oliver Kraft, and Cynthia A. Volkert ultrahigh-strength-single-crystalline-nanowhiskers-grown-by-physical-vapor-deposition. *Nano Letters* **2009**, *9*, 3048–3052.

[39] Raegen, A. N.;Yin, J.;Zhou, Q.; Forrest, J. A. Ultrastable monodisperse polymer glass formed by physical vapour deposition. *Nature Materials* **2020**, *19*, 1110-1113.

[40] Yuan, H.;Chen, Y.;Lin, R.;Tan, D.;Zhang, J.;Wang, Y.;Gazit, E.;Ji, W.; Yang, R. Modified Stranski-Krastanov Growth of Amino Acid Arrays toward Piezoelectric Energy Harvesting. *ACS Appl Mater Interfaces* **2022**, *14*, 46304-46312.

[41] Du, P.;Fan, W.;Gazit, E.;Tan, D.; Yang, R. Self-Assembly Behavior of Amino Acids on Au (111) Surfaces: A Molecular Dynamics Study. *Langmuir* **2026**, 10.1021/acs.langmuir.5c06072.

[42] Nguyen, V.;Zhu, R.;Jenkins, K.; Yang, R. Self-assembly of diphenylalanine peptide with controlled polarization for power generation. *Nat Commun* **2016**, *7*, 13566.

[43] Zhang, Z.;Li, X.;Peng, Z.;Yan, X.;Liu, S.;Hong, Y.;Shan, Y.;Xu, X.;Jin, L.;Liu, B.;Zhang, X.;Chai, Y.;Zhang, S.;Jen, A. K.; Yang, Z. Active self-assembly of piezoelectric biomolecular films via synergistic nanoconfinement and in-situ poling. *Nat Commun* **2023**, *14*, 4094.

[44] Bera, S.;Guerin, S.;Yuan, H.;O'Donnell, J.;Reynolds, N. P.;Maraba, O.;Ji, W.;Shimon, L. J. W.;Cazade, P.-A.;Tofail, S. A. M.;Thompson, D.;Yang, R.; Gazit, E. Molecular engineering of piezoelectricity in collagen-mimicking peptide assemblies. *Nature Communications* **2021**, *12*.

Electronic Supplementary Material

Vapor-phase self-assembly of orientation-controlled amino acid nanorod arrays for energy harvesting

Ying Tang[1,2,§], Pei Du[2,§], Shuaikang Zhou[2], Tong Wu[2], Weiqiang Fan[2], Haoyu Wang[2], Ehud Gazit[3], and Rusen Yang[1] (✉)

[1] *School of Physics, Xidian University, Xi'an 710071, China*
[2] *School of Advanced Materials and Nanotechnology, Xidian University, Xi'an 710071, China*
[3] *Department of Molecular Microbiology and Biotechnology, George S. Wise Faculty of Life Sciences, Tel Aviv University, Tel Aviv 6997801, Israel*
[§] *Ying Tang and Pei Du contributed equally to this study.*

Supporting information to https://doi.org/10.26599/NR.2026.94908745

Table S1. Calculated Young's modulus of L-Tyr. (E)(GPa)

Averaging scheme	Young's modulus
Voigt	E_V = 18.795 GPa
Reuss	E_R = 17.912 GPa
Hill	E_H = 18.354 GPa

Table S2. Calculated elastic stiffness tensor **C**, piezoelectric stress coefficient tensor **e**, and piezoelectric charge coefficient tensor **d** for L-Tyr.

Tensor type	Tensor Expression
The elastic stiffness constant of L-Tyr. (GPa)	$\begin{pmatrix} 18.635 & 3.352 & 5.548 & 0 & 0 & 0 \\ 3.352 & 12.207 & 4.686 & 0 & 0 & 0 \\ 5.548 & 4.686 & 26.317 & 0 & 0 & 0 \\ 0 & 0 & 0 & 9.439 & 0 & 0 \\ 0 & 0 & 0 & 0 & 9.174 & 0 \\ 0 & 0 & 0 & 0 & 0 & 5.405 \end{pmatrix}$
The piezoelectric stress coefficient **e** of L-Tyr. (C m^{-2})	$\begin{pmatrix} 0 & 0 & 0 & -0.03436 & 0 & 0 \\ 0 & 0 & 0 & 0 & -0.09997 & 0 \\ 0 & 0 & 0 & 0 & 0 & -0.05652 \end{pmatrix}$
The piezoelectric charge coefficient **d** of L-Tyr. (pm V^{-1})	$\begin{pmatrix} 0 & 0 & 0 & -4.20821 & 0 & 0 \\ 0 & 0 & 0 & 0 & -19.5751 & 0 \\ 0 & 0 & 0 & 0 & 0 & -6.19873 \end{pmatrix}$

Table S3. Deposition parameters for aromatic amino acids.

Material	Substrate temperature	Source temperature	Deposition time
L-Phe	80 °C	110 °C	1 h
L-Tyr	80 °C	160 °C	1 h
L-DOPA	80 °C	200 °C	1 h

Table S4. Comparison of representative amino-acid-based piezoelectric materials and nanogenerators reported in previous studies and this work.

Material	Fabrication method	Piezoelectric coefficient	Output performance	Mechanical property	Ref.
L-Val	PVD	11.4 pm V^{-1}	0.84 V (Voc)	/	[40]
β-glycine film	nanoconfinement and in-situ poling	11.2 pm V^{-1}	14.5 V (Voc), 4 μA(Isc)	/	[43]
Cbz-pentafluoro-Phe	solution method	2.0 pm V^{-1}	/	/	[24]
Pro-Phe-Phe	solution method	2.15 pm V^{-1}	1.4 V (Voc), 52nA(Isc)	/	[44]
Ordered L-tyrosine array	**PVD**	**3.62 pm V^{-1}**	**0.8 V (Voc), 110 nA (Isc)**	**Young's modulus: 16.96 ± 0.05 GPa**	**This work**

Note : The reported piezoelectric coefficients and output performances were collected from the literature. Since different characterization methods, device structures, and testing conditions were used in different studies, these values are presented mainly for qualitative and relative comparison. The output performance listed here corresponds to the representative electrical output parameters reported in the original articles. Mechanical properties are listed only when explicitly reported in the corresponding references.

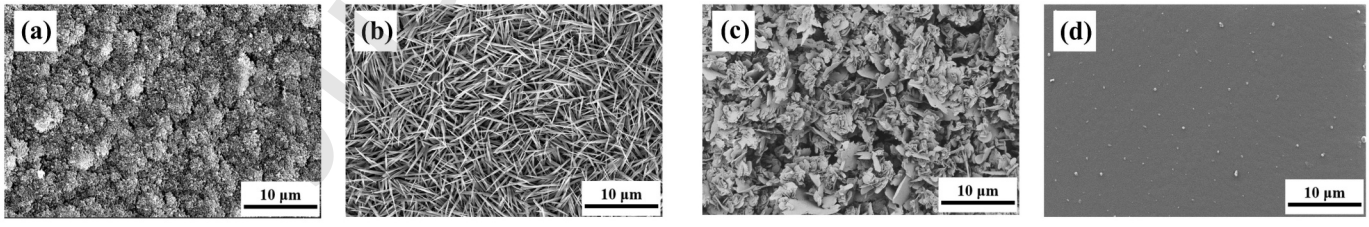

Figure S1. SEM characterization of the self-assembled crystalline thin films of aromatic amino acids via PVD. (a) L-Phe: The SEM image shows relatively uniform granular structures. (b) L-Tyr: Well-defined needle-like structures are observed. (c) L-Trp: The film exhibits more complex sheet-like morphologies. (d) L-Dopa: A smooth and highly uniform thin-film morphology is obtained.
For all samples, the substrate temperature was maintained at 80 °C during deposition. The source temperatures were 110 °C for L-Phe, 160 °C for L-Tyr, 170 °C for L-Trp, and 200 °C for L-Dopa, respectively.

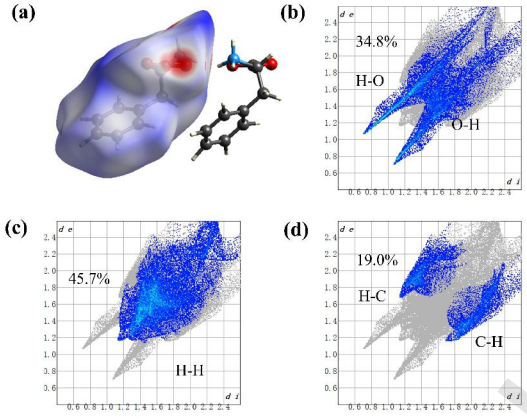

Figure S2. Hirshfeld surface analysis of L-Phe. (a) Hirshfeld surface plot. (b-d) 2D fingerprint plots derived using the parameter dnorm, showing the contribution of O-H (b), H-H (c), and C-H (d).

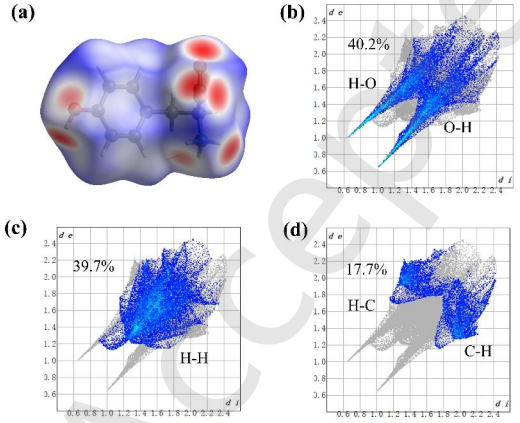

Figure S3. Hirshfeld surface analysis of L-Tyr. (a) Hirshfeld surface plot. (b-d) 2D fingerprint plots derived using the parameter dnorm, showing the contribution of O-H (b), H-H (c), and C-H (d).

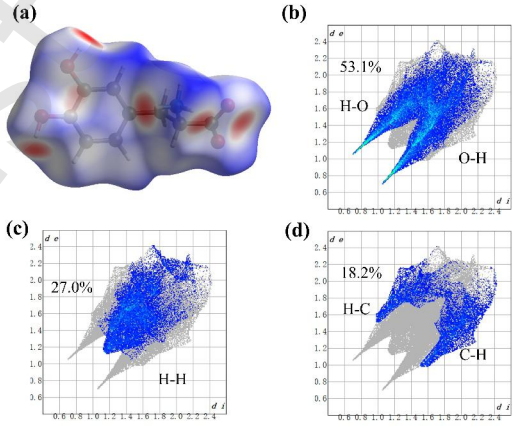

Figure S4. Hirshfeld surface analysis of L-Dopa. (a) Hirshfeld surface plot. (b-d) 2D fingerprint plots generated using the parameter dnorm, showing the contribution of O-H (b), H-H (c), and C-H (d).

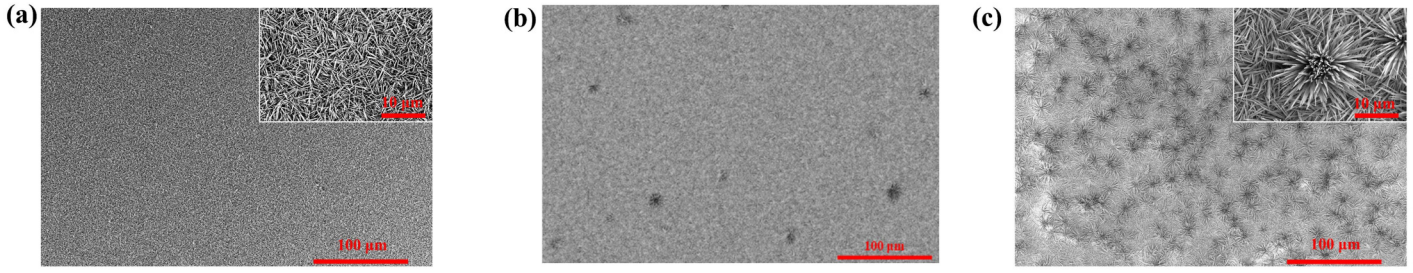

Figure S5. SEM images showing the effect of the applied electric field on the morphology of L-Tyr arrays during PVD at 80 °C: (a) without an applied electric field, (b) with an applied voltage of 1 kV, and (c) with an applied voltage of 2 kV..

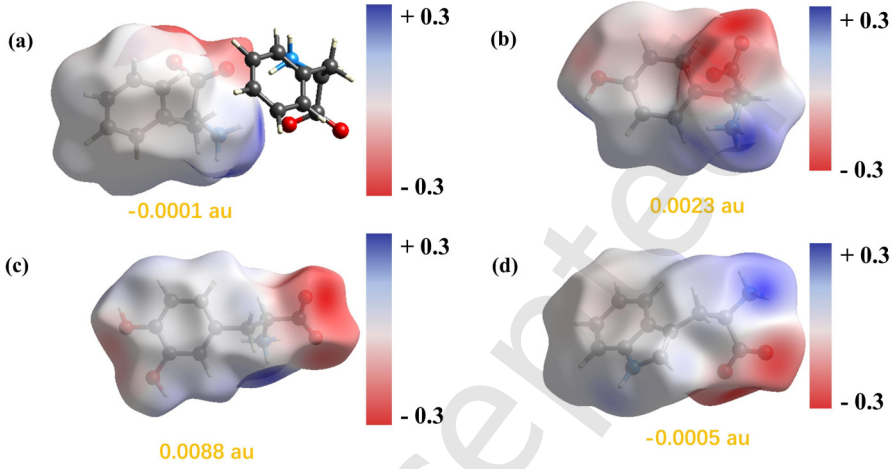

Figure S6. Comparison of intermolecular electrostatic potentials mapped on Hirshfeld surfaces in the range of +0.3 au (blue) to −0.3 au (red) for (a) L-Phe, (b) L-Tyr, (c) L-Trp, and (d) L-Dopa molecules.

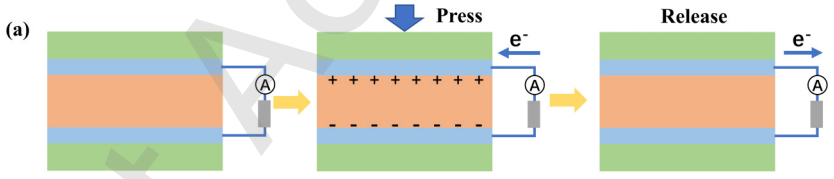

Figure S7. Schematic diagram of the energy conversion process of a piezoelectric nanogenerator.

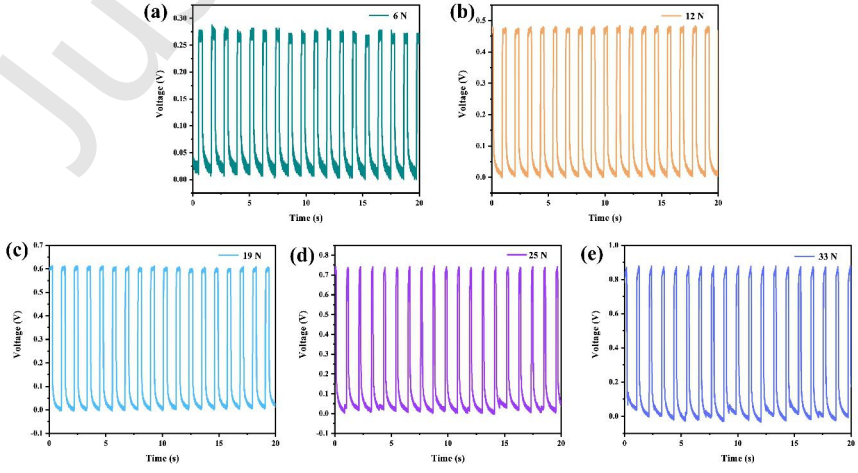

Figure S8. Output voltage obtained from an L- tyrosine- based nanogenerator under different applied forces of 6 N (a), 12 N (b), 19 N (c), 25 N (d), and33 N (e).

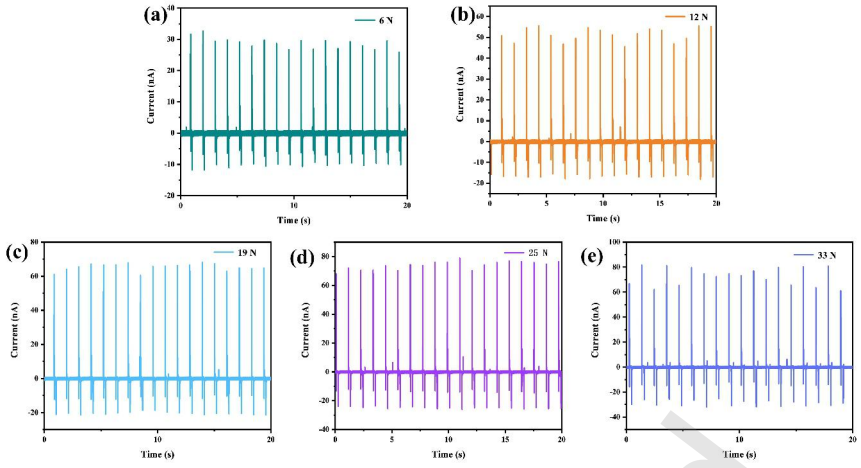

Figure S9. Output current from an L- Tyr- based nanogenerator under different applied forces of 6 N (a), 12 N (b), 19 N (c), 25 N (d), and 33 N (e).

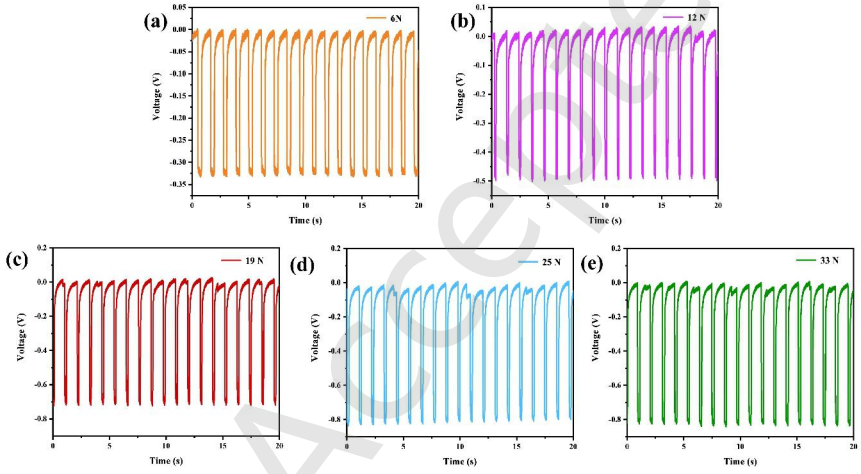

Figure S10. Output voltage from an L- Tyr- based nanogenerator under different applied forces of 6 N (a), 12 N (b), 19 N (c), 25 N (d), and 33 N (e) with reversed connections.

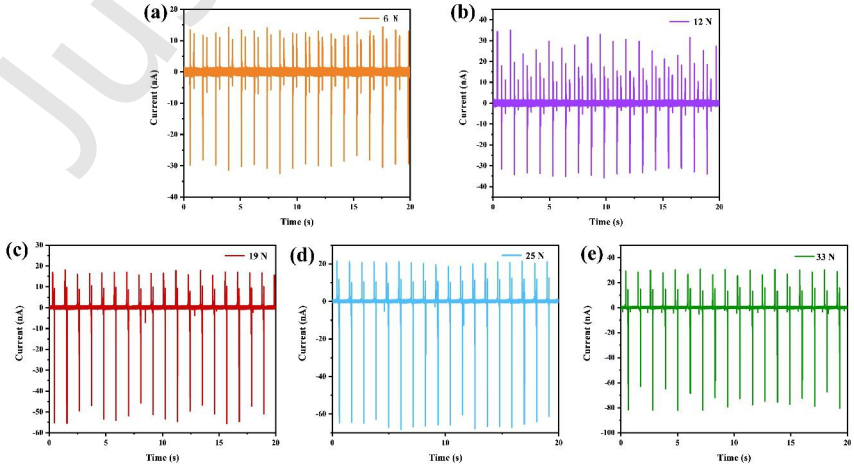

Figure S11. Output current obtained from the L- tyrosine- based nanogenerator under different applied forces of 6 N (a), 12 N (b), 19 N (c), 25 N (d), and 33 N (e) with reversed connections.

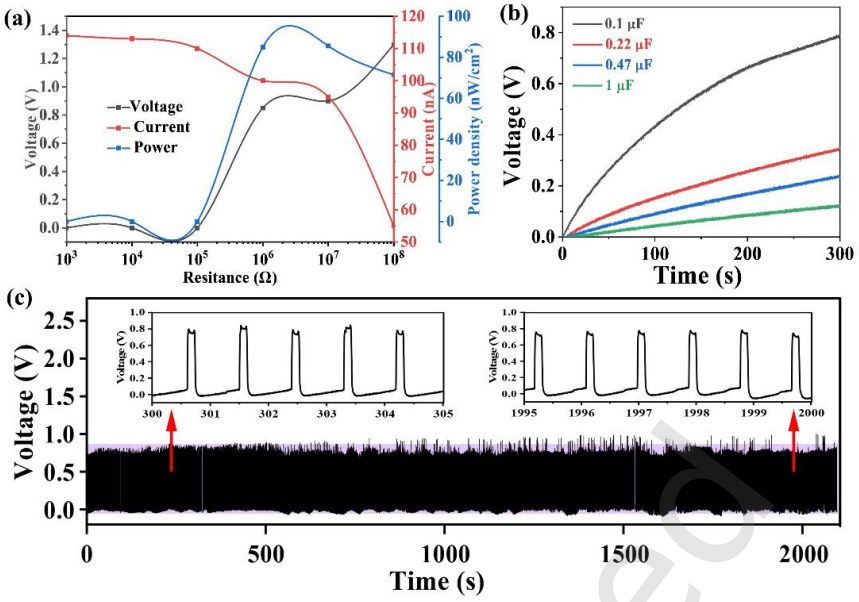

Figure S12. (a) Power density of the L-tyrosine-based nanogenerator under different external loads; (b) Charging curves of capacitors with different capacitances charged by the L-tyrosine-based nanogenerator; (c) Cycling stability of the L-tyrosine-based nanogenerator over time.